Building a free-energy functional from atomically resolved imaging: Atomic-scale phenomena in La-doped $BiFeO_3$

Anna N. Morozovska,[1] Eugene A. Eliseev,[2] Deyang Chen,[3] Christopher T. Nelson,[4] and Sergei V. Kalinin[4,*]

[1]*Institute of Physics, National Academy of Sciences of Ukraine, 46, pr. Nauky, 03028 Kyiv, Ukraine*

[2]*Institute for Problems of Materials Science, National Academy of Sciences of Ukraine, Krjijanovskogo 3, 03142 Kyiv, Ukraine*

[3]*Institute for Advanced Materials and Guangdong Provincial Key Laboratory of Optical Information Materials and Technology, South China Academy of Optoelectronics, South China Normal University, Guangzhou 510006, China*

[4]*The Center for Nanophase Materials Sciences, Oak Ridge National Laboratory, Oak Ridge, Tennessee 37831, USA*

(Received 6 April 2019; published 22 May 2019; corrected 1 June 2020)

Scanning transmission electron microscopy (STEM) has enabled mapping of atomic structures of solids with sub-picometer precision, providing insight to the physics of ferroic phenomena and chemical expansion. However, only a subset of information is available, due to projective nature of imaging in the beam direction. Correspondingly, the analysis often relies on the postulated form of macroscopic Landau-Ginzburg energy for the ferroic long-range order parameter, and some predefined relationship between experimentally determined atomic coordinates and the order-parameter field. Here, we propose an approach for exploring the structure of ferroics using reduced order-parameter models constructed based on experimental data only. We develop a four-sublattice model (FSM) for the analytical description of *A*-cation displacement in (anti)ferroelectric-antiferrodistortive perovskites of ABO_3 type. The model describes the displacements of cation *A* in four neighboring unit cells and determines the conditions of different structural phases' appearance and stability in ABO_3. We show that FSM explains the coexistence of rhombohedral, orthorhombic, and spatially modulated phases, observed by atomic-resolution STEM in La-doped $BiFeO_3$. Using this approach, we atomically resolve and theoretically model the sublattice asymmetry inherent to the case of the *A*-site La/Bi cation sublattice in $La_xBi_{1-x}FeO_3$ polymorphs. This approach allows the exploration of ferroic behaviors from experimental data only, without additional assumptions on the nature of the order parameter.

DOI: 10.1103/PhysRevB.99.195440

I. INTRODUCTION

Ferroic materials are the object of continuous fascination for the condensed-matter physics community. For over 50 years, the properties of these systems were explored using the combination of scattering techniques that provided the information on the nature and symmetry of corresponding order parameters, and macroscopic property measurements that provided the information on the corresponding expansion coefficients and the nature of phase transitions [1–7]. Once available, the free-energy expansion in powers of order parameter(s) is employed in Landau-Ginsburg-Devonshire (LGD) free energy [8], and can further be used in the phase-field modeling of macro- and nanosized ferroelectrics [9]. Obviously, the nature of boundary conditions at surfaces and interfaces were typically postulated, in the form of (poorly known) correlation and screening lengths [8–10]. Consequently, this approach worked relatively poorly for systems such as polar nanoregions and nanodomains in relaxor ferroelectrics [1], morphotropic systems, or the atomic-scale alternation of polarization in antiferroelectrics and modulated phases [2].

Understanding of ferroic behavior at surfaces, interfaces, and defects as well as the nature of ferroelectric states, considerably advanced in the last decades, with the advancement of (scanning) transmission electron microscopy [(S)TEM for short] [3–6]. Probing the unit-cell level symmetry breaking via STEM allowed the determination of direct atomic positions [4,11–13], from which the spatial distributions of order-parameter fields can be mapped. However, these analyses to date have been based on two fundamental assumptions. Namely, the nature of the order parameter was assumed to be that of one of the bulk phases of the material. Secondly, the relationship between the experimentally measured atomic coordinates and the order parameter was postulated via certain *ad hoc* models [10,14].

Here we derive a model LGD-type free energy describing directly observable degrees of freedom available from atomic-resolution STEM. We propose a theoretical four-sublattice model (FSM for short) for the analytical description of cation displacement in (anti)ferroelectric-antiferrodistortive perovskites of ABO_3 type, that explain the coexistence of rhombohedral (*R*), orthorhombic (*O*), and spatially modulated (*SM*) phases observed by atomic-resolution STEM. Using this approach, we atomically resolve and theoretically model the sublattice asymmetry inherent to the case of the *A*-site La/Bi cation sublattice in perovskite $La_xBi_{1-x}FeO_3$ polymorphs.

II. EXPERIMENTAL RESULTS

As a model system, we use bismuth ferrite (BFO) solid solution. BFO itself is a multiferroic with high ferroelectric Curie temperature $T_C = 1100\,\mathrm{K}$ and antiferromagnetic Néel

*sergei2@ornl.gov

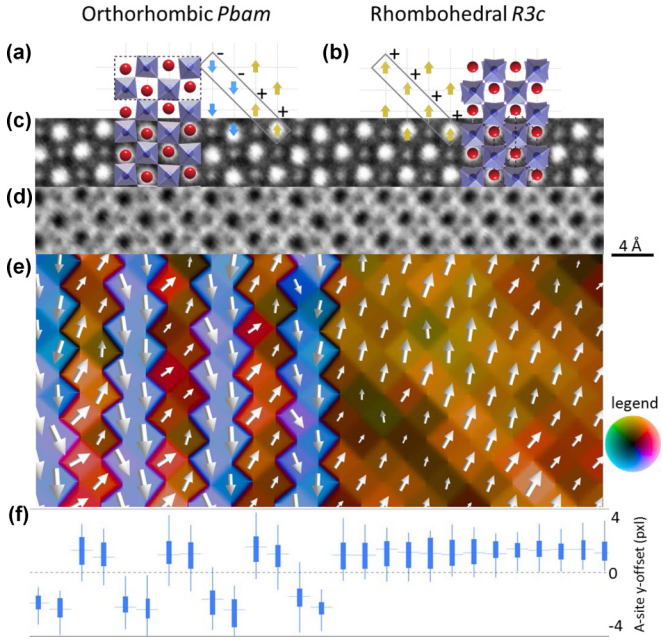

FIG. 1. STEM of the $La_{0.17}Bi_{0.83}FeO_3$. The interface between the orthorhombic *O* (left) and rhombohedral *R* (right) phases is shown. (a) Atomic model of the *O-Pbam* antiferroelectric type structure $++-\,-$ [2]. (b) Atomic model of the rhombohedral ferroelectric *R*3*c* structure $+\,+\,+\,+$ [17]. (c) Atomic-resolution HAADF image. (d) Atomic resolution ABF image. (e)*A*-site displacements. (f). Box and whisker plot of the [101] displacement component per layer (∼35 datapoints per column).

temperature $T_N = 650$ K, high remanent ferroelectric polarization ($\sim 90\,\mu C/cm^{-2}$) along the [111] axis, and antiferromagnetic order coexisting at room temperatures [15,16]. In addition to the rhombohedral *R*3*c* host phase [17], there are numerous polymorphs experimentally identified in BFO, including epitaxial strain-stabilized ferroelectric tetragonal [18], monoclinic [19], and orthorhombic phases [20], as well as a rare-earth dopant-stabilized orthorhombic *Pbam* or *Pnma* phases of antiferroelectric type [21–26] (such as in $PbZrO_3$), which exhibit a high piezoelectric response at the morphotropic phase boundary (MPB) [23].

Here we explore the MPB of $La_xBi_{1-x}FeO_3$ (BFO:La), when 17% La doping stabilizes a phase coexistence between the host ferroelectric rhombohedral and orthorhombic phases at room temperature. The precise space group is not elucidated here but our prior experiments showed projected atomic positions in STEM images isostructural to *Pbam* $PbZrO_3$ as well as antiferroelectric behavior by *P-E* double loops [21]. Both of these phases exhibits a large principal displacive polar distortion of the La/Bi *A* site from the pseudocubic position; for the *O* phase this consists of the in-plane displacements on alternating pairs of $[101]_{pseudocubic}$ planes in a "++ −− ++…"-type pattern [Fig. 1(a)], whereas for the ferroelectric *R*3*c* phase this consists of displacements along the [111] polarization direction resulting in a uniformly polarized "++++…" pattern [Fig. 1(b)].

Here, $La_{0.17}Bi_{0.83}FeO_3$ thin films were fabricated on $SrRuO_3/SrTiO_3$ sublayer deposited on Si substrates using pulsed laser deposition. The films exhibit coexistence of ferroelectric *R*3*c* [Fig. 1(a)] and antiferroelectric *O* phases [Fig. 1(b)] with phase boundaries forming preferentially on [101] planes [21]. STEM images centered at one such boundary are shown for the *high-angle annular dark-field* (HAADF) and *annular bright-field* (ABF) detectors [see Fig. 1(c) and Fig. 1(d), respectively], the former with bright atom contrast sensitive to the atom column *Z*, and the latter an approximately dark atom contrast image with higher sensitivity to light elements like oxygen. The difference in structure, especially the *A*-site sublattice displacements [Fig. 1(e)], is readily apparent even from the raw HAADF and ABF images. The [101] plane bisecting the figure contains both the alternating +[101] and −[101] directions of the *A*-site distortions of the *Pbam* phase, as well as the [−1,±1,−1] direction of the *R*3*c* phase distortions. In this manner the boundary mimics the local antiferroelectric distortion inherent to the *Pbam* phase. From the [101] displacement statistics vs distance normal to the interface [Fig. 1(f)] the interface appears atomically sharp within experimental error bars.

The dataset in Fig. 1(e) was derived from a single HAADF image and, therefore, subject to scanning artifacts from positional drift during the slow raster of the electron probe over the area of interest. The result is significantly higher error in relative positions for vertically offset features (the slow-scan axis) compared with horizontal features. As a result, the image was corrected along the vertical axis for dilation and shear measured as *x*-axis-correlated variation of atomic spacing from the global mean. *XY* positions of *A*- and *B*-site cations were determined by Gaussian fit. *Y*-axis corrections were smoothed (via a spline fit) and the local transform was applied as a best fit to minimize the variation from the global mean.

Foremost, the high atomic numbers *(Z)* of the *A*-site cations ($Z_{Bi} = 83$, $Z_{La} = 57$) compared to *B*-site cations ($Z_{Fe} = 26$) and oxygen ($Z_O = 8$) lead to the dominant contribution of *A* site to the HAADF signal, and thus they exhibit a much higher signal-to-noise ratio and lower atom positioning error [13]. Moreover, assuming chemical homogeneity on the *A*-site columns, the probe incident on adjacent *A* sites exhibits similar scattering environments with respect to channeling, etc. The result is that experimental measurements of the *A* site in isolation have considerably smaller error and greater robustness against artifacts such as from off-axis tilt [27] compared to positional noncentrosymmetry analysis that also incorporates Fe or O sublattices. There is a potential point of uncertainty in utilizing the isolated *A*-site sublattice as in some cases the centrosymmetric reference point can be ill defined. If, for instance, the images in Fig. 1 contain only a uniform *R*3*c* phase, from the *A*-site positions alone the displacement magnitudes are unknown, and so the ++++ ferroelectric and 0000 paraelectric phases cannot be distinguished. Thus, the *B*-cation sublattice is useful for establishing a reference lattice to measure the *A* site and was the method used for the dataset in Fig. 1(e).

III. THEORETICAL DESCRIPTION

Here we describe the FSM in accordance with experimental results, shown in Fig. 1. The conventional LGD free-energy density is a sum of Landau, gradient, and surface energies:

$$G = \int_V (G_{\text{Landau}} + G_{\text{grad}}) + G_S. \tag{1a}$$

Landau free-energy expansion, containing the quadratic and bilinear contributions of the A-cations' displacements A_i ($i = 1-4$) in ABO_3 perovskite with $m3m$ parent phase, is

$$\begin{aligned} G_{\text{Landau}} = {} & \frac{\alpha}{2}A_iA_i + \mu(A_1A_2 + A_2A_3 + A_3A_4 + A_1A_4) \\ & + \eta(A_1A_3 + A_2A_4) + \frac{\beta}{4}A_i^2A_i^2 \\ & + \frac{\gamma}{2}\left(A_1^2A_2^2 + A_2^2A_3^2 + A_3^2A_4^2 + A_1^2A_4^2\right) \\ & + \frac{\delta}{2}\left(A_1^2A_3^2 + A_2^2A_4^2\right) + \lambda A_1A_2A_3A_4 + \ldots. \end{aligned} \tag{1b}$$

Here we assume that only the first term in Eq. (1b) has a temperature-dependent coefficient, namely $\alpha = \alpha_T(T - T_C)$, and all constants can depend on the global or local content of impurity (e.g., La atoms).

The atomic displacements of different sublattices (which are equivalent in undoped ABO_3) could be considered as long-range order parameters, A_1, A_2, A_3, and A_4. We further assume that the standard inequality $\frac{\beta}{4} > \frac{\gamma}{2} > \frac{\delta}{2} \gg \lambda$ is valid, as necessary for the functional stability and expansion series convergence.

The gradient energy $G_{\text{grad}} = g_{ijkl}\frac{\partial A_i}{\partial x_k}\frac{\partial A_j}{\partial x_l}$ will be considered in the simplest isotropic approximation for the gradient coefficient tensor g_{ijkl}, and that all physical quantities are x dependent:

$$G_{\text{grad}} = g_{ijkl}\frac{\partial A_i}{\partial x_k}\frac{\partial A_j}{\partial x_l} \approx g\left(\frac{\partial A_i}{\partial x}\right)^2. \tag{1c}$$

The surface energy is assumed to be a positively defined quadratic form,

$$G_S = \frac{\alpha_S}{2}\left(A_1^2 + A_2^2 + A_3^2 + A_4^2\right). \tag{1d}$$

Using Dzyaloshinsky substitution [28]

$$\begin{aligned} B_1 &= \frac{A_1 + A_2 + A_3 + A_4}{2}, \quad B_2 = \frac{A_1 - A_2 - A_3 + A_4}{2}, \\ B_3 &= \frac{A_1 - A_2 + A_3 - A_4}{2}, \quad B_4 = \frac{A_1 + A_2 - A_3 - A_4}{2} \end{aligned} \tag{2}$$

and making elementary algebraic transformation listed in the Supplemental Material [29], one could rewrite Eq. (1b) as follows:

$$\begin{aligned} G_{\text{Landau}} = {} & \frac{\alpha^*}{2}B_1^2 + \frac{\mu^*}{2}\left(B_2^2 + B_4^2\right) + \frac{\eta^*}{2}B_3^2 \\ & + \frac{\beta^*}{4}\left(B_1^4 + B_2^4 + B_3^4 + B_4^4\right) \\ & + \gamma^*\left(B_1^2B_2^2 + B_2^2B_3^2 + B_3^2B_4^2 + B_1^2B_4^2\right) \\ & + \frac{\delta^*}{4}\left(B_2^2B_4^2 + B_1^2B_3^2\right) + \lambda^*B_1B_2B_3B_4. \end{aligned} \tag{3a}$$

The expansion coefficients are

$$\begin{aligned} &\alpha^* = \alpha + 2\mu + \eta, \quad \mu^* = \alpha - \eta, \quad \eta^* = \alpha - 2\mu + \eta, \\ &\beta^* = \frac{\beta}{4} + \frac{\gamma}{2} + \frac{\delta}{4} + \frac{\lambda}{4}, \quad \gamma^* = \frac{3\beta}{8} + \frac{\gamma}{4} - \frac{\delta}{8} - \frac{\lambda}{8}, \\ &\delta^* = \frac{3\beta}{2} - \gamma + \frac{3\delta}{2} - \frac{\lambda}{2}, \quad \lambda^* = \frac{3\beta}{2} - \gamma - \frac{\delta}{2} + \frac{\lambda}{2}. \end{aligned} \tag{3b}$$

Under the condition $\lambda^* > 0$, expression (3a) contains several possible phase transitions from the paraelectric phase to the different homogeneous phases (R and O) or spatially modulated phases (SM I, II, III), which are listed in Table I.

To model the boundary between coexisting R, O, and SM phases, one can solve numerically coupled Euler-Lagrange equations obtained by the variation of the free energy (3). The equations are supplemented by the third-kind boundary conditions (BCs) steming from the surface energy variation with respect to the cation displacements (see the Supplemental Material [29] for details). Being interested in the coexistence of different phases in a thin ABO_3 film, we compared the limiting cases of zero BCs, $B_i|_{x=0,h} = 0$, with natural BCs, $\frac{\partial B_i}{\partial x}|_{x=0,h} = 0$, and conditions of the components' periodicity in a bulk sample.

Since the coefficients α, β, γ, λ, δ, μ, and η in the stability conditions depend on the impurity content in the solid solution, the appearance of O and R phases and their coexistence can be explained. The gradient terms and higher terms, or both can make the modulation in O and SM phases much more complicated.

Formally, R and O phases coexistence (that is observed by STEM) can be realized in the case of their energies equality. The coexistence condition, $G_R = G_O$, gives $\alpha - \eta = \alpha + 2\mu + \eta \Leftrightarrow -\eta = \mu$ per Table I, and the phase stability conditions are $\alpha + 2\mu + \eta < 0$, $\alpha - \eta < 0$, and $\beta + 2\gamma + \delta + \lambda > 0$.

In the case of the weak deviations from the phase equilibrium, $-\eta = \mu$, i.e., when the condition $\eta + \mu + \varsigma = 0$ takes place along with the inequality $|\varsigma| \ll \mu$, one could write the free energy (3) in the following dimensionless form:

$$\begin{aligned} G_{12} \approx -(\alpha + \mu)B_S^2\int_V \Bigg[& -(1-c)\frac{b_1^2}{2} - (1+c)\frac{b_2^2}{2} + \frac{b_1^4 + b_2^4}{4} \\ & + \frac{\chi}{2}b_1^2b_2^2 + \frac{h}{2}\left(\left(\frac{\partial b_1}{\partial x}\right)^2 + \left(\frac{\partial b_2}{\partial x}\right)^2\right)\Bigg], \end{aligned} \tag{4}$$

where the order parameters $B_i = B_S b_i$ ($i = 1,2$), the spontaneous value $B_S = 2\sqrt{-\frac{\alpha+2\mu+\eta}{\beta+2\gamma+\delta+\lambda}}$, dimensionless coupling constant $\chi = (\frac{3\beta}{4} + \frac{\gamma}{2} - \frac{\delta}{4} - \frac{\lambda}{4})(\frac{\beta}{4} + \frac{\gamma}{2} + \frac{\delta}{4} + \frac{\lambda}{4})^{-1}$, and gradient coefficient $h = B_S^2 g$ are introduced (see the Supplemental Material [29] for the details of calculations). The parameter $c \equiv \frac{\varsigma}{\alpha+\mu}$ is the sublattice asymmetry constant.

Thus, FSM reduces the description of R and O phases' coexistence to the thermodynamic analyses of the free-energy functional with three dimensionless phenomenological parameters—asymmetry constant c, sublattices coupling strength χ, and order parameter gradient energy coefficient h. R phase corresponds to $b_1 \neq 0$ and $b_2 = 0$, while O phase corresponds to $b_2 \neq 0$ and $b_1 = 0$.

To study the boundary between coexisting R and O phases, we solved numerically coupled Euler-Lagrange equations obtained by the variation of the energy (4) supplemented by the natural BCs, $\frac{\partial b_i}{\partial x}|_{x=0,h} = 0$, and conditions of the components' periodicity in a bulk sample.

Distribution of order parameters b_1 and b_2 near the boundary between R domain (left) and O domain (right) are shown in Fig. 2. It is seen from Fig. 2(a) that the increase of the

TABLE I. Description of different homogeneous phases in Eqs. (1)–(3) and necessary conditions of their stability.

Phase name	Signs of $A_1A_2A_3A_4$	Values of the order parameters B_i and A_i	Necessary conditions and corresponding energy value
Para phase	0000	$B_1=0, B_2=0, B_3=0, B_4=0$	$\frac{\alpha}{2}-\lvert\mu\rvert+\frac{\eta}{2}\geqslant 0, \frac{\alpha}{2}-\frac{\eta}{2}\geqslant 0$
	$----$	$A_1=0, A_2=0, A_3=0, A_4=0$	$G_P=0$
Homogeneous (R phase)	$++++$	$B_1=\sqrt{-\frac{\alpha^*}{\beta^*}}, B_2=0, B_3=0, B_4=0$	$\alpha+2\mu+\eta<0,$
		$A_1=A_2=A_3=A_4=\sqrt{-\frac{\alpha^*}{4\beta^*}}$	$\beta+2\gamma+\delta+\lambda>0 \quad G_R=\frac{-\alpha^{*2}}{\beta^*}$
Modulated I (O phase)	$+--+$ or	$B_2=\sqrt{-\frac{\mu^*}{\beta^*}}$, (or the same B_4)	$\alpha-\eta<0,$
	$-++-$	$B_1=0, B_3=0, B_4=0$ (or $B_2=0$)	$\beta+2\gamma+\delta+\lambda>0, G_O=\frac{-\mu^{*2}}{4\beta^*}$
		$A_1=A_2=-A_3=-A_4=\sqrt{-\frac{\mu^*}{4\beta^*}}$	
Modulated II (AFE phase)	$+-+-$	$B_1=0, B_2=0, B_4=0, B_3=\sqrt{-\frac{\eta^*}{\beta^*}},$	$\alpha-2\mu+\eta<0$
		$A_1=-A_2=A_3=-A_4=\sqrt{-\frac{\eta^*}{4\beta^*}}$	$\beta+2\gamma+\delta+\lambda>0 \quad G_A=\frac{-\eta^{*2}}{4\beta^*}$
Modulated III (mixture of several phases)	$+0-0$	$B_2=B_4=\sqrt{-\frac{\alpha-\eta}{\beta+\delta}}, B_1=0, B_3=0,$	$\alpha-\eta<0, \beta+\delta>0,$
		$A_1=-A_3=\frac{1}{2}\sqrt{-\frac{\alpha-\eta}{\beta+\delta}}, A_2=A_4=0$	$G_M=\frac{-(\alpha-\eta)^2}{4(\beta+\delta)}$

dimensionless coupling constant χ leads to the narrowing of the interfacial region between R and O phases. Actually, the higher is the term $\frac{\chi}{2}b_1^2b_2^2$, the stronger is the coupling between the dimensionless order parameters b_1 and b_2. For a weak coupling corresponding to $\chi<1$, two separate R and O phases are unstable [and the case is not shown in the Fig. 2(a)]. As one can see from Fig. 2(b) the increase of the sublattice asymmetry parameter c supports R phase with $b_2=0$. In particular, the saturation value of b_1 decreases and tends to disappear with further increase of c. At the same time, the width of the interfacial R-O region is almost unaffected by the variation of the parameter c. Note that c value can be regarded proportional to the impurity concentration, while χ and h are regarded as concentration independent.

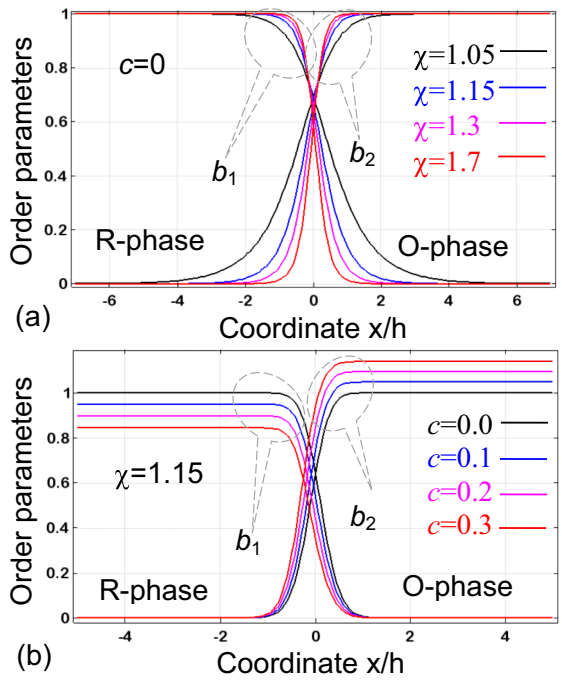

FIG. 2. Distribution of order parameters b_1 and b_2 near the interface between R phase (left) and O phase (right) (a) for $c=0$ and different values of parameter $\chi=1.05$, 1.15, 1.3, and 1.7 (black, blue, magenta, and red curves, respectively); (b) for $\chi=1.15$ and different values of parameter $c=0$, 0.1, 0.2, and 0.3 (black, blue, magenta, and red curves, respectively).

IV. COMPARISON WITH EXPERIMENT

Although the order parameters B_i are very convenient for the theoretical description of the phase diagram, their distribution cannot be observed directly in STEM experiments, while the distribution of the order parameters A_i indeed can. The distribution of the normalized order parameters A_1 and A_2 near the boundary between R domain (left) and O domain (right) are shown in Fig. 3. Let us compare Fig. 3 with experimental results shown at the bottom of Fig. 1(e). As one can see, the semiquantitative agreement is present between Fig. 3 and Fig. 1(e) because $A_1\approx A_2\approx A_3\approx A_4$ in R domain, while the value of $A_1\approx A_2$ and $A_3\approx A_4$ change their signs in O domain.

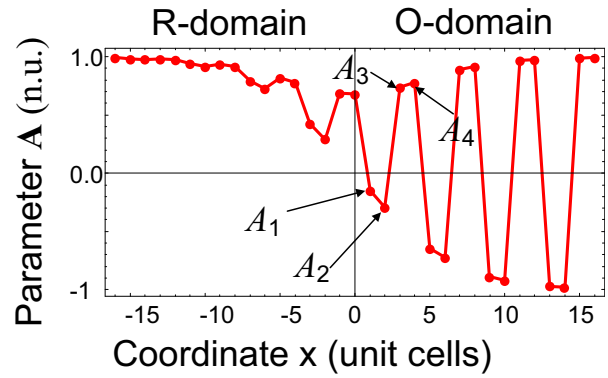

FIG. 3. Distribution of the normalized order parameters A_i (in cyclic order) near the boundary between R domain (left) and O domain (right).

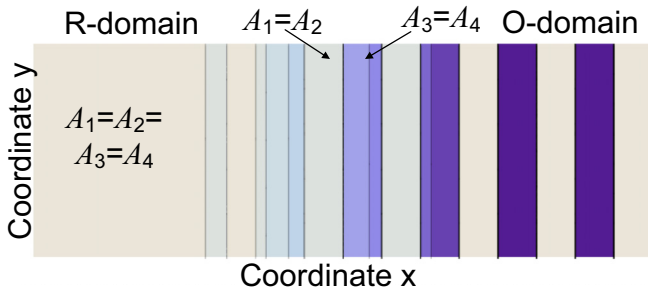

FIG. 4. Cations A-displacement map according to theoretical calculations near the boundary between R domain (left) and O domain (right).

Cations A displacement map near the phase boundary between R and O domain has been calculated theoretically and shown in Fig. 4. Note the evident agreement between the theoretical Fig. 4 and experimental results shown in Figs. 1(e) and 1(f), because the contrast is absent in R domain, where $A_1 \approx A_2 \approx A_3 \approx A_4$, while it is alternating in O domain, where the values of $A_1 \approx A_2$ and $A_3 \approx A_4$ change their signs.

V. CONCLUSION

We propose a LGD-type free energy describing the displacements of A-cation sublattices in (anti)ferroelectric-antiferrodistortive perovskites of ABO_3-type. The four sublattices model, four-sublattice model (FSM) for short, proposes analytical description of the A-cation displacements in four neighboring cells and determines the conditions of different (O, R, and SM) phase appearance and stability in pristine and doped ABO_3-type perovskites. Thus FSM explains the atomic displacements in La-doped BFO we observed by atomic-resolution STEM measurements.

FSM reduces the description of R and O phase coexistence to the thermodynamic analyses of the free-energy functional with three dimensionless parameters, such as sublattice asymmetry constant c, their coupling strength χ, and gradient energy coefficient h. Increase of the constant χ leads to the narrowing of the interface region between R and O phases. For a weak coupling between sublattices (corresponding to $\chi<1$) two separate R and O phases become unstable. The increase of the asymmetry parameter c supports R phase. At the same time, the width of the interfacial R-O region is almost unaffected by the variation of the parameter c. Note that c value can be proportional to La concentration in BFO, while χ and h are regarded as concentration independent.

The FSM model has the advantage of deriving from a directly observable order parameter in atomic-scale STEM measurements. For the large A-site displacive type Pb- or Bi-based (anti)ferrodistortive-(anti)ferroelectrics [like (Bi, La)FeO_3 or Pb(Ti, Zr)O_3] this method also maximizes the experimental precision, as it derives exclusively from the strongest scattering atomic columns undergoing the largest displacements from their centrosymmetric positions within a unit cell.

ACKNOWLEDGMENTS

The authors are very grateful to the referee for excellent suggestions how to improve the form of Dzyaloshinsky substitution. This material is based upon work (S.V.K., C.T.N.) supported by the US Department of Energy, Office of Science, Office of Basic Energy Sciences, Materials Sciences and Engineering Division, and performed in the Center for Nanophase Materials Sciences, supported by the Division of Scientific User Facilities. The work of A.N.M. has received funding from the European Union's Horizon 2020 research and innovation program under the Marie Skłodowska-Curie Grant Agreement No. 778070, and partially supported by the National Academy of Sciences of Ukraine (Project No. 0117U002612). D.C. thanks the financial support from the National Natural Science Foundation of China (Grants No. U1832104 and No. 11704130).

Authors' contribution. A.N.M. and E.A.E. proposed the theoretical model and performed calculations. D.C. performed the LBFO film PLD synthesis. C.T.N. performed and analyzed the STEM experiments. S.V.K. generated the research idea, interpreted theoretical and experimental results and wrote the manuscript draft. All co-authors worked on the results discussion and manuscript improvement.

[1] H. Takenaka, I. Grinberg, S. Liu, and A. M. Rappe, Slush-like polar structures in single-crystal relaxors, Nature (London) **546**, 391 (2017).

[2] S. Teslic and T. Egami, Atomic structure of $PbZrO_3$ determined by pulsed neutron diffraction, Acta Crystallogr. B **54**, 750 (1998).

[3] D. D. Fong, G. B. Stephenson, S. K. Streiffer, J. A. Eastman, O. Auciello, P. H. Fuoss, and C. Thompson, Ferroelectricity in ultrathin perovskite films, Science **304**, 1650 (2004).

[4] A. K. Yadav, C. T. Nelson, S. L. Hsu, Z. Hong, J. D. Clarkson, C. M. Schlepütz, A. R. Damodaran, P. Shafer, E. Arenholz, L. R. Dedon, and D. Chen, Observation of polar vortices in oxide superlattices, Nature (London) **530**, 198 (2016).

[5] C. T. Nelson, P. Gao, J. R. Jokisaari, C. Heikes, C. Adamo, A. Melville, S.-H. Baek, C. M. Folkman, B. Winchester, Y. Gu, and Y. Liu, Domain dynamics during ferroelectric switching, Science **334**, 968 (2011).

[6] A. Gruverman, O. Auciello, and H. Tokumoto, Scanning force microscopy for the study of domain structure in ferroelectric thin films, J. Vac. Sci. Technol. B **14**, 602 (1996).

[7] H. Lu, C.-W. Bark, D. Esque De Los Ojos, J. Alcala, C.-B. Eom, G. Catalan, and A. Gruverman, Mechanical writing of ferroelectric polarization, Science **336**, 59 (2012).

[8] A. F. Devonshire, XCVI. Theory of barium titanate: Part I, London, Edinburgh, Dublin Philos. Mag. J. Sci. **40**, 1040 (1949).

[9] L.-Q. Chen, Phase-field method of phase transitions/domain structures in ferroelectric thin films: A review, J. Am. Ceram. Soc. **91**, 1835 (2008).

[10] Q. Li, C. T. Nelson, S.-L. Hsu, A. R. Damodaran, L.-L. Li, A. K. Yadav, M. McCarter, L. W. Martin, R. Ramesh, and S. V. Kalinin, Quantification of flexoelectricity in $PbTiO_3/SrTiO_3$ superlattice polar vortices using machine learning and phase-field modeling, Nat. Commun. **8**, 1468 (2017).

[11] C.-L. Jia, V. Nagarajan, J.-Q. He, L. Houben, T. Zhao, R. Ramesh, K. Urban, and R. Waser, Unit-cell scale mapping of ferroelectricity and tetragonality in epitaxial ultrathin ferroelectric films, Nat. Mater. **6**, 64 (2007).

[12] A. K. Yadav, K. X. Nguyen, Z. Hong, P. García-Fernández, P. Aguado-Puente, C. T. Nelson, S. Das, B. Prasad, D. Kwon, S. Cheema, and A. I. Khan, Spatially resolved steady-state negative capacitance, Nature (London) **565**, 468 (2019).

[13] C. T. Nelson, B. Winchester, Y. Zhang, S.-J. Kim, A. Melville, C. Adamo, C. M. Folkman. S. H. Baek, C. B. Eom, D. G. Schlom, and L. Q. Chen, Spontaneous vortex nanodomain arrays at ferroelectric heterointerfaces, Nano Lett. **11**, 828 (2011).

[14] K. Aoyagi, T. Kiguchi, Y. Ehara, T. Yamada, H. Funakubo, and T. J. Konno, Diffraction contrast analysis of 90° and 180° ferroelectric domain structures of $PbTiO_3$ thin films, Sci. Technol. Adv. Mater. **12**, 034403 (2011).

[15] J. B. N. J. Wang, J. B. Neaton, H. Zheng, V. Nagarajan, S. B. Ogale, B. Liu, D. Viehland, V. Vaithyanathan, D. G. Schlom, U. V. Waghmare, and N. A. Spaldin, Epitaxial $BiFeO_3$ multiferroic thin film heterostructures, Science **299**, 1719 (2003).

[16] P. Fischer, M. Polomska, I. Sosnowska, and M. Szymanski, Temperature dependence of the crystal and magnetic structures of $BiFeO_3$, J. Phys. C: Solid State Phys. **13**, 1931 (1980).

[17] F. Kubel and H. Schmid, Structure of a ferroelectric and ferroelastic monodomain crystal of the perovskite $BiFeO_3$, Acta Crystallogr. B **46**, 698 (1990).

[18] R. J. Zeches, M. D. Rossell, J. X. Zhang, A. J. Hatt, Q. He, C.-H. Yang, A. Kumar, C. H. Wang, A. Melville, C. Adamo, and G. Sheng, A strain-driven morphotropic phase boundary in $BiFeO_3$, Science **326**, 977 (2009).

[19] H. Béa, B. Dupé, S. Fusil, R. Mattana, E. Jacquet, B. Warot-Fonrose, F. Wilhelm, A. Rogalev, S. Petit, V. Cros, A. Anane, F. Petroff, K. Bouzehouane, G. Geneste, B. Dkhil, S. Lisenkov, I. Ponomareva, L. Bellaiche, M. Bibes, and A. Barthélémy, Evidence for Room-Temperature Multiferroicity in a Compound with a Giant Axial Ratio, Phys. Rev. Lett. **102**, 217603 (2009).

[20] J. C. Yang, Q. He, S. J. Suresha, C. Y. Kuo, C. Y. Peng, R. C. Haislmaier, M. A. Motyka, G. Sheng, C. Adamo, H. J. Lin *et al.*, Orthorhombic $BiFeO_3$, Phys. Rev. Lett. **109**, 247606 (2012).

[21] D. Chen, C. T. Nelson, X. Zhu, C. R. Serrao, J. D. Clarkson, Z. Wang, Y. Gao, S.-L. Hsu, L. R. Dedon, Z. Chen, D. Yi, H.-J. Liu, D. Zeng, Y.-H. Chu, J. Liu, D. G. Schlom, and R. Ramesh. A strain-driven antiferroelectric-to-ferroelectric phase transition in La-doped $BiFeO_3$ thin films on Si, Nano Lett. **17**, 5823 (2017).

[22] C. S. Knee, M. G. Tucker, P. Manuel, S. Cai, J. Bielecki, L. Börjesson, and S. G. Eriksson, High pressure crystal and magnetic phase transitions in multiferroic $Bi_{0.9}La_{0.1}FeO_3$, Chem. Mater. **26**, 1180 (2014).

[23] S. Fujino, M. Murakami, V. Anbusathaiah, S.-H. Lim, V. Nagarajan, C. J. Fennie, M. Wuttig, L. Salamanca-Riba, and I. Takeuchi, Combinatorial discovery of a lead-free morphotropic phase boundary in a thin-film piezoelectric perovskite, Appl. Phys. Lett. **92**, 202904 (2008).

[24] A. Y. Borisevich, E. A. Eliseev, A. N. Morozovska, C.-J. Cheng, J.-Y. Lin, Y.-H. Chu, D. Kan, I. Takeuchi, V. Nagarajan, and S. V. Kalinin, Atomic-scale evolution of modulated phases at the ferroelectric–antiferroelectric morphotropic phase boundary controlled by flexoelectric interaction, Nat. Commun. **3**, 775 (2012).

[25] D. Kan, L. Pálová, V. Anbusathaiah, C. J. Cheng, S. Fujino, V. Nagarajan, K. M. Rabe, and I. Takeuchi, Universal behavior and electric-field-induced structural transition in rare-earth-substituted $BiFeO_3$, Adv. Funct. Mater. **20**, 1108 (2010).

[26] C.-J. Cheng, D. Kan, S.-H. Lim, W. R. McKenzie, P. R. Munroe, L. G. Salamanca-Riba, R. L. Withers, I. Takeuchi, and V. Nagarajan, Structural transitions and complex domain structures across a ferroelectric-to-antiferroelectric phase boundary in epitaxial Sm-doped $BiFeO_3$ thin films, Phys. Rev. B **80**, 014109 (2009).

[27] P. Gao, A. Kumamoto, R. Ishikawa, N. Lugg, N. Shibata, and Y. Ikuhara, Picometer-scale atom position analysis in annular bright-field STEM imaging, Ultramicroscopy **184**, 177 (2018).

[28] I. Dzyaloshinsky, A thermodynamic theory of "weak" ferromagnetism of antiferromagnetics, J. Phys. Chem. Solids, **4**, 241 (1958).

[29] See Supplemental Material at http://link.aps.org/supplemental/10.1103/PhysRevB.99.195440 for the free-energy calculation details.

Correction: Missing material in the Acknowledgment section has been inserted.